Optimized Active Disturbance Rejection Control With Resonant Extended State Observer for Grid Voltage Sensorless *LCL*-Filtered Inverter

Thuy Vi Tran, Kyeong-Hwa Kim, *Senior Member, IEEE*, and Jih-Sheng Lai, *Life Fellow, IEEE*

***Abstract*—A robust optimized active disturbance rejection control (ADRC) based grid voltage sensorless current controller is developed for an *LCL*-filtered grid-connected inverter (GCI) via a predictive control approach under various sources of disturbance, including the model uncertainties, the *LCL* inherent resonance phenomenon, and nonideal grid environment. Aiming to improve the sinusoidal reference tracking performance as well as to reject lumped sinusoidal disturbances in the control practice, a resonant extended state observer is integrated into the ADRC structure, which guarantees a rigorous stable operation of inverter for bounded filter parameter uncertainties and adverse grid voltage conditions. The grid frequency adaptability is thoroughly considered in the controller design process and synchronization technique, offering an extra capability for GCI to operate under different grid voltage frequency levels or even the frequency deviation caused by grid fault events. Robustness against parameter uncertainty and system stability is analyzed through the discrete-time frequency analysis and pole-zero map approaches. The simulation and hardware experiments are conducted for GCI with *LCL* filter parameters designed for two typical regions (i.e., the resonance frequency is less and greater than one-sixth of switching frequency) to validate the theoretical analysis and the effectiveness of the proposed control method.**

***Index Terms*—Active disturbance rejection control (ADRC), generalized predictive control (GPC), *LCL*-filtered grid-connected inverter (GCI), resonant extended state observer (RESO), uncertainties and disturbances, voltage sensorless control.**

I. Introduction

NOWADAYS the intensive utilization of voltage-source inverter (VSI) for interfacing the power sources with the unity grid is observed along with the rapid development in smart grid and renewable energy-based distributed generation systems. In industrial applications, high-performance grid-connected inverter (GCI) systems should be achieved in views of good quality grid-injected currents and a reliable operation under several unexpected conditions. To meet the grid connection standard requirements, the *LCL*-type filters are commonly adopted to attenuate the high switching frequency. In comparison with other filter types, such as *L* or *LC*, the *LCL* filter offers a better harmonic suppression capability. However, it requires more attention in controller design to damp the inherent resonance phenomenon of *LCL* filter by passive [1] or active [2], [3] manners. Besides, since the physical system uncertainties and the external disturbances always exist, the controller design for GCI to ensure satisfactory output performance is a challenging task. Particularly, the *LCL* filter parameter variations, which come from the aging-induced degradation or the grid impedance variation in the weak grid, cause negative effects or even destabilize the operation of inverter controllers as well as the damping strategies that rely on the accurate system model [4], [5]. To avoid the degradation of the active damping (AD) method under weak grid condition, the AD method is further developed with the capacitor current and grid voltage feedback to obtain a stable system for a wide grid inductance variation [6]. Another method in [7] presents the weighted average current strategy to suppress the resonance phenomenon and a separate-structure uncertainty and disturbance estimator to improve the system robustness under a weak grid. However, both approaches still require extra sensors to measure the filter capacitor or inverter-side currents. The grid voltages are considered as the external disturbance input to the GCI system. To fulfill the objective of injecting high-quality active power to the main grid, the controller is required to be robust even if the grid environment contains unbalanced and distorted harmonics, or the grid frequency varies during grid fault events. Those adverse factors should be taken into consideration in the high-performance GCI current controller design process.

To inject high-quality currents under unbalanced grid voltages into the main grid, a fast phase capture scheme to extract the positive and negative sequences of unbalanced grid voltages is associated with the conventional current regulator for *LCL*-filtered GCI in [8]. Otherwise, the control approaches in [9] and [10] demonstrate their effective operations with the *L*- and *LCL*-filtered prototypes, respectively, under unbalanced grid voltages and the filter parameter variations by means of

Manuscript received February 1, 2021; revised March 29, 2021; accepted May 17, 2021. Date of publication May 24, 2021; date of current version July 30, 2021. This work was supported in part by the Basic Science Research Program through the National Research Foundation of Korea funded by the Ministry of Education under Grant NRF-2019R1A6A1A03032119 and in part by the National Research Foundation of Korea grant funded by the Korea government (MSIT) under Grant NRF-2020R1F1A1048262. Recommended for publication by Associate Editor M. Liserre. *(Corresponding author: Kyeong-Hwa Kim.)*

Thuy Vi Tran and Kyeong-Hwa Kim are with the Department of Electrical and Information Engineering, Research Center for Electrical and Information Technology, Seoul National University of Science and Technology, Seoul 01811, South Korea (e-mail: tranvithuy@gmail.com; k2h1@seoultech.ac.kr).

Jih-Sheng Lai is with the Future Energy Electronics Center, Department of Electrical and Computer Engineering, Virginia Polytechnic Institute and State University, Blacksburg, VA 24061 USA (e-mail: laijs@vt.edu).

Color versions of one or more figures in this article are available at https://doi.org/10.1109/TPEL.2021.3082938.

Digital Object Identifier 10.1109/TPEL.2021.3082938

the combination of the uncertainty and disturbance observers (DOBs), and current controllers. Other control schemes in [11] design a robust state feedback current controller in which the system uncertainties and possible time-varying system parameters are considered by solving the linear matrix inequalities. Even though the evaluation results of the above schemes demonstrate strong robustness under severe test conditions, those approaches still require additional sensors to measure the capacitor currents for damping the resonance phenomenon of the *LCL* filter. The application of robust current controllers, such as an enhanced Lyapunov-function-based control and the sliding-mode control, is studied in [12] and [13], respectively, to deal with several perturbation sources as distorted unbalanced grid and system parameter uncertainties. However, the requirement of extra filter capacitor voltage sensors in [12] and the multiple sliding surface formations in [13] increases the system cost as well as controller and hardware complexity.

Various control approaches for GCI have been investigated in the literature not only to obtain the high-quality injected currents but also to reduce the system complexity by adopting the sensorless operation. In particular, the full-state feedback control with augmenting multiple control terms to deal with the distorted grid is presented in [14] and [15]. Even though those schemes successfully realize the grid voltage sensorless operation, they require the accurate power inverter model; thus, the output currents are quite sensitive to uncertainties. In [16], the Lyapunov energy function-based control and multiple estimators are presented to verify the capability of eliminating the grid voltage sensors or current sensors under adverse grid voltage conditions. Although the analytical results show a small degradation of the model-based estimators with the filter resistance and inductance variation up to 200% from their nominal values, a large set of grid impedance under a weak grid has not been considered. Another approach in [17] achieves a robust AD algorithm against the grid inductance change by means of a sliding-mode control for an *L*-filter model, which is used to simplify the actual model of the *LCL* filter. The stability of the system is well validated under large grid impedance variations; however, it is noticed that since the inverter-side current is chosen as the controlled object, the resonance phenomenon may still happen if the grid-side current is directly controlled. The finite control set model predictive control (MPC) and a sliding-mode observer-based control are presented in [18] and [19], respectively. Owing to robust current control schemes and multiple observers to estimate both the grid voltages and state variables, those approaches successfully stabilize the *LCL*-filtered GCIs under both internal and external perturbations with only grid-side current sensor installation. However, all robust control schemes mentioned above have not taken the grid frequency variation into consideration as one of the major disturbance sources during grid faults.

Recently, there is a particular focus on estimating and eliminating disturbance influences in the physical inverter systems, which has been reported in several approaches, such as the unknown input observer (UIO) based scheme [15], the DOB based current controller [20], and the active disturbance rejection control (ADRC) with extended state observer (ESO) [21], [22]. Since the UIO-based control scheme is originally constructed to estimate the external disturbance only (i.e., the grid voltage disturbances), the internal uncertainty has not been considered yet. On the other hand, the DOB-based controller [20] formulates the inverse of the nominal plant transfer function to estimate the unknown plant dynamic as well. However, the requirement of two separated observers to accomplish the control objectives in this approach raises a concern of heavy computational burden.

The development of ESO in the ADRC concept proposed in [23] and [24] is also based on the state-space approach as UIO. However, the lumped internal and external disturbance estimation sets the ADRC apart from the conventional counterpart. In the GCI application, a linear ADRC-based direct current control is implemented in the stationary frame [21] and the synchronous reference frame (SRF) in [25] and [26] to deal with the *LCL* resonance phenomenon and uncertainty in filter circuits. By means of the ESO to estimate the output and its derivatives as well as the lumped disturbance, the desired control performance can be achieved by a simple linear state feedback control algorithm with online disturbance rejection. Although those schemes show favorable results under a large range of filter parameter variations, the time delay in the digital implementation is not considered in [21], and the unexpected grid environment still challenges the control operation in [25] and [26].

The traditional ESO with one extended state ensures the asymptotical estimation convergence of states and the constant or slowly varying disturbance, which is an advantageous feature for the control scheme built in SRF. However, in case the current controller is constructed in the stationary frame, the total disturbance is in the form of the sinusoidal signal. It raises the difficulty for the original ADRC scheme to completely reject the disturbance and track the reference with high precision. This problem is reported in the ADRC-based speed controller of permanent magnet synchronous motor (PMSM) [27] in which a proportional resonant (PR) regulator is utilized instead of a proportional controller to combine the merits of ADRC and PR controller for compensating both constant and time-varying disturbances. Although the presented approach provides good results for the first-order ADRC of the PMSM speed control, the application for higher order plant as the *LCL*-filtered inverter has not been studied. A higher order linear ESO is developed in [28], known as generalized ESO, to improve the tracking performance of time-varying disturbance. However, it is also not appropriate to model the disturbance with an infinitely differentiable form as the sinusoid. Furthermore, since the higher order ESO model will narrow down the system stability margin, the order of ESO should be considered carefully for each application [29]. The resonant extended state observer (RESO) is first presented in [30] in the continuous-time domain to overcome the challenge of lumped sinusoidal disturbance. This scheme is experimentally verified on the three-axis didactic radar platform. The modified ESO with an integrated sinusoidal disturbance model tuned at a fixed resonance frequency enables the asymptotic convergence of both state and disturbance estimations.

To pursue the high-performance current controller for the *LCL*-filtered GCI, an optimized ADRC-based current controller is developed in this article. Aiming to fully eliminate the negative

effects from grid voltage disturbances and internal disturbances caused by model uncertainties in the GCI system, a frequency adaptive RESO and harmonic compensators are combined with the ADRC-based controller, which achieves the objective of output current tracking and disturbance rejection. Furthermore, a least-mean-square-based frequency estimator technique is adopted to extract the grid synchronization information from the estimated disturbance of RESO, providing a grid voltage sensorless operation. Inspired by the generalized predictive control (GPC) method [31]–[33], an optimal control input is derived by minimizing a receding-horizon performance index instead of utilizing the pole placement method to select the feedback gains of ADRC-based controller [21], [26]. Since the future information of the proposed scheme is achieved by the Taylor expansion, the optimal control law is offline explicitly derived; thus, the heavy online computational burden of the conventional MPC is avoided. The contributions of this article are as follows.

1) The current controller of the *LCL*-filtered GCI is developed based on the ADRC framework, where the proposed frequency adaptive RESO is constructed in form of the discrete current-type estimator to eliminate the system delay caused by the digital implementation.
2) The control law via GPC is derived for the third-order *LCL*-filtered GCI to form an optimal robust current control scheme.
3) The following adverse disturbance sources are taken into account in the design process: distorted and unbalanced grid voltages, grid frequency variations, filter circuit uncertainties, and weak grid with identical or different grid impedance values among three phases.
4) The robustness against the internal and external disturbances, together with the stability of the proposed approach, is investigated through the discrete-time frequency analysis and pole-zero map approach.

The feasibility and effectiveness of the proposed scheme are verified by simulation and experiments with fair comparisons to the conventional approach to demonstrate the performance of the proposed scheme.

II. System Description

A three-phase GCI configuration is represented in Fig. 1, which includes the dc-link capacitor, VSI, and *LCL* filter. In this figure, the *LCL* filter is constituted by the inverter-side inductor L_1, the grid-side inductor L_2, and the filter capacitor C_f, while L_g is the grid inductor to represent the weak grid condition. The system state variables including the inverter-side currents, grid-side currents, and capacitor voltages are defined as i_1^x, i_2^x, and v_c^x (superscript x represents the reference frame of variables), respectively. The inverter voltage v_i^x and grid voltage v_d^x measured at the point of common coupling (PCC) play the role of a control input and a disturbance of the GCI system, v_g^x is the actual grid voltage behind the grid inductor L_g. It should be noted that all parasitic resistances of L_1, L_2, and L_g are ignored to consider the worst case of zero passive damping.

The objective of the current controller is to provide the high-quality grid-injected currents even in the presence of various

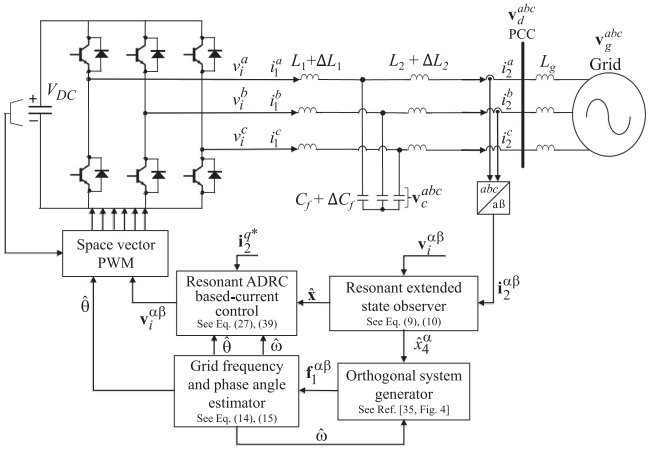

Fig. 1. Control block diagram of the *LCL*-filtered GCI system with the proposed current control scheme.

internal disturbances caused by parameter uncertainties and external disturbances from the grid. To improve the robustness of the GCI and obtain good reference tracking performance, a resonant-ADRC-based current control combining the RESO is employed. In the proposed control structure, multiple resonant controllers tuned at the low-order harmonics of the grid are adopted as an effective method to maintain good output currents from the severe distorted grid. Meanwhile, the ADRC-based controller associated with RESO plays the main role to deal with the unbalanced grid voltages and internal uncertainties.

Generally, the grid synchronization task is accomplished by means of the phase-locked loop (PLL) with the measured voltages at PCC, which are distorted or unbalanced under adverse grid conditions. Therefore, for the purpose of not only eliminating the grid voltage sensors but also overcoming those negative effects, the grid frequency and phase angle estimator are presented to extract the grid voltage information from estimated disturbances.

A. Model of GCI System

The linear dynamic model of the inverter system in the stationary frame is given for the α- and β-axis as follows:

$$L_1' i_1^{\alpha\beta(1)}(t) = v_i^{\alpha\beta}(t) - v_c^{\alpha\beta}(t) \tag{1}$$

$$C_f' v_c^{\alpha\beta(1)}(t) = i_1^{\alpha\beta}(t) - i_2^{\alpha\beta}(t) \tag{2}$$

$$L_2' i_2^{\alpha\beta(1)}(t) = v_c^{\alpha\beta}(t) - v_d^{\alpha\beta}(t) \tag{3}$$

where superscript (n) describes the nth time derivative, $L_1' = L_1 + \Delta L_1$, $L_2' = L_2 + \Delta L_2$, and $C_f' = C_f + \Delta C_f$, the prime symbol denotes the actual uncertain system parameter, and Δ is the parameter error between the actual and nominal quantities.

B. Integral Chain Form of GCI System

The key idea that makes the ADRC approach apart from the conventional schemes is to consider both internal disturbances and external disturbances as a lumped disturbance, which is estimated by an observer and eliminated in real time via the control

input [23], [24]. To facilitate the idea, the uncertain inverter model is first transformed to the integral chain form, in which the system output of the grid-side current, first-order derivative term, and second-order derivative term in the stationary frame are expressed as follows [21]:

$$x_1^{\alpha\beta} = i_2^{\alpha\beta} \tag{4}$$

$$x_2^{\alpha\beta} = x_1^{\alpha\beta(1)} = \frac{1}{L_2'}\left(v_c^{\alpha\beta} - v_d^{\alpha\beta}\right) \tag{5}$$

$$x_3^{\alpha\beta} = x_2^{\alpha\beta(1)} = \frac{1}{L_2'}\left(v_c^{\alpha\beta(1)} - v_d^{\alpha\beta(1)}\right) = \frac{1}{L_2'C_f'}\left(i_1^{\alpha\beta} - i_2^{\alpha\beta}\right) - \frac{1}{L_2'}v_d^{\alpha\beta(1)} \tag{6}$$

$$x_3^{\alpha\beta(1)} = \frac{1}{L_1'L_2'C_f'}\left(v_i^{\alpha\beta} - v_c^{\alpha\beta}\right) - \frac{1}{L_2'^2C_f'}\left(v_c^{\alpha\beta} - v_d^{\alpha\beta}\right) - \frac{1}{L_2'}v_d^{\alpha\beta(2)}. \tag{7}$$

From (5)–(7), the integral chain form of the GCI system is presented in the state space as

$$\begin{bmatrix} x_1^{\alpha\beta(1)} \\ x_2^{\alpha\beta(1)} \\ x_3^{\alpha\beta(1)} \end{bmatrix} = \mathbf{A}\begin{bmatrix} x_1^{\alpha\beta} \\ x_2^{\alpha\beta} \\ x_3^{\alpha\beta} \end{bmatrix} + \mathbf{B}v_i^{\alpha\beta} + \mathbf{D}g^{\alpha\beta}$$

$$y^{\alpha\beta} = \mathbf{C}\begin{bmatrix} x_1^{\alpha\beta} & x_2^{\alpha\beta} & x_3^{\alpha\beta} \end{bmatrix}^T \tag{8}$$

where

$$\mathbf{A} = \begin{bmatrix} 0 & 1 & 0 \\ 0 & 0 & 1 \\ 0 & \eta & 0 \end{bmatrix}, \quad \mathbf{B} = \begin{bmatrix} 0 \\ 0 \\ b_o \end{bmatrix}, \quad \mathbf{D} = \begin{bmatrix} 0 \\ 0 \\ 1 \end{bmatrix}, \quad b_o = \frac{1}{L_1L_2C_f}, \quad \eta = -\left(\frac{1}{L_1C_f} + \frac{1}{L_2C_f}\right)$$

$$\mathbf{C} = \begin{bmatrix} 1 & 0 & 0 \end{bmatrix}, \quad g^{\alpha\beta} = g_e^{\alpha\beta}(v_d^{\alpha\beta}) + g_i^{\alpha\beta}(x_2^{\alpha\beta}, v_i^{\alpha\beta}, w)$$

$$g_e^{\alpha\beta}(v_d^{\alpha\beta}) = -\frac{1}{L_1'L_2'C_f'}v_d^{\alpha\beta} - \frac{1}{L_2'}v_d^{\alpha\beta(2)}$$

$$g_i^{\alpha\beta}(x_2^{\alpha\beta}, v_i^{\alpha\beta}, w) = \Delta\eta x_2^{\alpha\beta} + \Delta b_o v_i^{\alpha\beta} + w.$$

$g^{\alpha\beta}$ describes a lumped disturbance that includes internal disturbances of the system caused by parametric uncertainties $g_i^{\alpha\beta}(x_2^{\alpha\beta}, v_i^{\alpha\beta}, w)$, and the external disturbance $g_e^{\alpha\beta}(v_d^{\alpha\beta})$ from the grid voltages. Moreover, it is worth to define $\Delta\eta = -(\frac{1}{L_1'C_f'} + \frac{1}{L_2'C_f'}) - \eta$, $\Delta b_o = \frac{1}{L_1'L_2'C_f'} - b_o$ is caused by the *LCL* filter parameter mismatches, and w is the unknown dynamic.

III. Proposed Frequency Adaptive RESO

The proposed frequency adaptive RESO is employed to estimate both integral chain states and sinusoidal lumped disturbance. In this section, the RESO structure is presented in the discrete-time domain, and the grid voltage sensorless operation of the GCI system is elaborated.

A. Discrete Current-Type Frequency Adaptive RESO

Based on the measured grid-side currents, state variables $x_1^{\alpha\beta}$, $x_2^{\alpha\beta}$, and $x_3^{\alpha\beta}$ and a sinusoidal lumped disturbance are estimated by means of a RESO. The proposed RESO is constructed by augmenting a frequency adaptive sinusoidal model having the extended states $\hat{x}_4^{\alpha\beta}$ and $\hat{x}_5^{\alpha\beta}$ into the system model (8) in which the variable $\hat{x}_4^{\alpha\beta}$ is the estimated quantity of lumped disturbance $g^{\alpha\beta}$, and $\hat{x}_5^{\alpha\beta}$ is the auxiliary variable to form the sinusoidal model. Furthermore, to overcome the system delay caused by the digital implementation, the proposed observer is constructed in the discrete current-type form as follows [15], [28]:

$$\hat{\mathbf{x}}(k) = \bar{\mathbf{x}}(k) + \mathbf{L}(y^{\alpha\beta}(k) - \mathbf{H}\bar{\mathbf{x}}(k)) \tag{9}$$

$$\bar{\mathbf{x}}(k+1) = \mathbf{\Phi}\bar{\mathbf{x}}(k) + \mathbf{\Gamma}v_i^{\alpha\beta}(k) + \mathbf{\Phi}\mathbf{L}(y^{\alpha\beta}(k) - \mathbf{H}\bar{\mathbf{x}}(k)) \tag{10}$$

where $\hat{\mathbf{x}} = [\,\hat{x}_1^{\alpha\beta}\ \hat{x}_2^{\alpha\beta}\ \hat{x}_3^{\alpha\beta}\ \hat{x}_4^{\alpha\beta}\ \hat{x}_5^{\alpha\beta}\,]^T$ is the estimated state vector with a current time step update, $\bar{\mathbf{x}} = [\,\bar{x}_1^{\alpha\beta}\ \bar{x}_2^{\alpha\beta}\ \bar{x}_3^{\alpha\beta}\ \bar{x}_4^{\alpha\beta}\ \bar{x}_5^{\alpha\beta}\,]^T$ is the output from the predictive-type estimator.

$$\mathbf{\Phi} = \begin{bmatrix} & & & 0 & 0 \\ & \mathbf{A_{de}} & & 0 & 0 \\ & & & 1 & 0 \\ 0 & 0 & 0 & 2\cos(\hat{\omega}T_s) & 1 \\ 0 & 0 & 0 & -1 & 0 \end{bmatrix}, \quad \mathbf{\Gamma} = \begin{bmatrix} \\ \mathbf{B_{de}} \\ \\ 0 \\ 0 \end{bmatrix}$$

$$\mathbf{L} = \begin{bmatrix} l_1 \\ l_2 \\ l_3 \\ l_4 \\ l_5 \end{bmatrix}, \quad \mathbf{H} = \begin{bmatrix} 1 \\ 0 \\ 0 \\ 0 \\ 0 \end{bmatrix}^T.$$

$\mathbf{A_{de}}$ and $\mathbf{B_{de}}$ are the discretized counterparts of matrices $\mathbf{A}$ and $\mathbf{B}$, respectively, $\hat{\omega}$ is the estimated grid frequency obtained from the grid frequency estimator, and T_s is the sampling time. The current-type estimator gain vector $\mathbf{L}$ is designed to ensure that the discrete characteristic equation $|z\mathbf{I} - \mathbf{\Phi} + \mathbf{LH\Phi}|$ is asymptotically stable. It is noticed that the proposed observer form has the capability to update the frequency online, which ensures to maintain the stability of the observer even under the grid frequency variation. As a result, a RESO can be constructed by using (9) and (10) not only to estimate the system states $\hat{x}_1^{\alpha\beta}$, $\hat{x}_2^{\alpha\beta}$, and $\hat{x}_3^{\alpha\beta}$ but also to estimate the lumped disturbance term $g^{\alpha\beta}$ by means of the extended states $\hat{x}_4^{\alpha\beta}$ and $\hat{x}_5^{\alpha\beta}$ and a frequency adaptive sinusoidal model.

B. Inverter Synchronization by Estimated Disturbance

In (8), it is obvious that the lumped disturbance term $g^{\alpha\beta}$ is dominated by the component of $-v_d^{\alpha\beta}/L_1'L_2'C_f'$, which is exceedingly larger than the remaining terms, and contains the information on the grid frequency and phase angle. As a result, the estimated lumped disturbance $\hat{x}_4^{\alpha\beta}$ can be effectively utilized to accomplish the synchronization task. Clearly, the performance of the conventional PLL is severely degraded by the unbalanced inputs. Therefore, rather than utilizing both disturbance states of α and β axes to extract the grid information by the PLL approach,

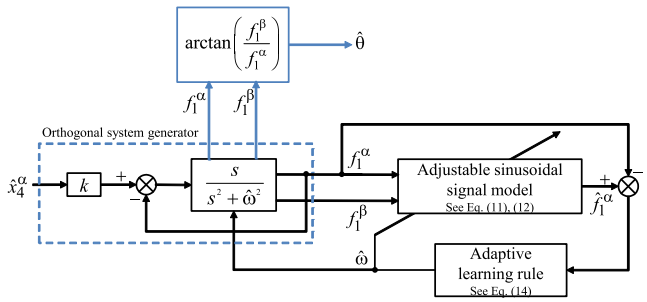

Fig. 2. Control block diagram of the grid frequency and phase angle estimator.

the estimator block diagram, as presented in Fig. 2, is implemented. The block diagram shows that only the disturbance state $\hat{x}_4^{\alpha}$ of the α-axis is fed to the proposed estimator through a gain factor k, while a balanced quadrature β-axis signal is regenerated via the orthogonal signal generator [34], [35]. This step provides the highly accurate estimation performance of grid frequency and phase angle even under unbalanced grid condition. The pure sinusoidal quantities from the orthogonal signal generator are fed to the least-mean-square-based grid frequency estimator to produce the estimated grid frequency and phase angle. These estimated parameters are used to adaptively adjust the current controller and RESO to avoid the performance degradation due to the mismatched frequency information.

The proposed grid frequency and phase angle estimator in Fig. 2 are mainly constructed by an adjustable sinusoidal signal model and an adaptive learning rule [35]. The adaptive learning rule is derived to produce the estimated grid frequency $\hat{\omega}$ with online for minimizing the estimation error between the reference sinusoidal signal f_1^{α} and the output of the adjustable sinusoidal signal model $\hat{f}_1^{\alpha}$. Generally, the output of the adjustable sinusoidal signal model having the estimated frequency $\hat{\omega}$ as oscillation frequency is presented in the discrete-time domain as

$$\hat{f}_1^{\alpha}(k+1) = f_1^{\alpha}(k) - \hat{\omega} T_s f_1^{\beta}(k) \tag{11}$$

$$\hat{f}_1^{\beta}(k+1) = f_1^{\beta}(k) + \hat{\omega} T_s f_1^{\alpha}(k). \tag{12}$$

It can be implied from (11) and (12) that the signal $\hat{f}_1^{\alpha}$ well converges to f_1^{α} as the estimated frequency $\hat{\omega}$ reaches close to the actual ω. Thus, an adaptive learning rule is developed based on the least-mean-square algorithm to minimize the estimation parameter error $e_f(k)$, defined as [36]

$$e_f(k) = \hat{f}_1^{\alpha}(k) - f_1^{\alpha}(k). \tag{13}$$

From (13), the adaptive learning rule to estimate $\hat{\omega}$ is calculated iteratively using the following:

$$\hat{\omega}(k+1) = \hat{\omega}(k) + \frac{\gamma T_s f_1^{\beta}(k-1) e_f(k)}{\varepsilon + \left[T_s f_1^{\beta}(k-1)\right]^2} \tag{14}$$

where γ is an adaption gain and ε is a small value to avoid the division by zero.

Finally, for the synchronization purpose, the estimated grid phase angle is directly derived from the outputs of the orthogonal signal generator using the following:

$$\hat{\theta} = \arctan\left(\frac{f_1^{\beta}}{f_1^{\alpha}}\right). \tag{15}$$

The effectiveness of the proposed synchronization technique is demonstrated in Section V.

IV. Optimized Resonant-ADRC-Based Current Controller

In this section, an optimized resonant-ADRC-based reference tracking problem is solved to ensure that the output current of the perturbed GCI system asymptotically tracks a reference. To study the robustness and the stability of the proposed approach, a two-degree-of-freedom (2-DOF) internal model control structure [37], [38] is developed for the proposed control scheme in the discrete-time domain. It is noted that since the system model in the α-axis and β-axis is independent, the current controller can be designed for the α-axis, then applied it for the β-axis without the loss of generality.

A. ADRC-Based Controller Design

Inspired by the generalized MPC proposed by Chen *et al.* [31], a generalized performance index with the tracking error consideration is introduced for the GCI system as follows:

$$J = \frac{1}{2}\int_0^{T_P} \left[\breve{y}^*(t+\tau) - \breve{y}(t+\tau)\right]^2 d\tau \tag{16}$$

where T_P is the predictive period, $\breve{y}$ is the prediction of the inverter output y^{α}, and $\breve{y}^*$ is the prediction of the output current reference $y^{\alpha *}$ within the horizon time interval.

It is noted that the relative degree of the *LCL*-filtered GCI system is 3, where the relative degree is the number of differentiations of the inverter output current y^{α} before the control input v_i^{α} appears explicitly. By means of the Taylor series expansion, the future output $\breve{y}$ and its reference $\breve{y}^*$ of the GCI system with the relative degree of 3 are presented as

$$\begin{aligned}\breve{y}(t+\tau) &\approx y^{\alpha}(t) + \tau y^{\alpha(1)}(t) + \cdots + \frac{\tau^{3+r}}{(3+r)!} y^{\alpha(3+r)}(t) \\ &= \Im(\tau)\mathbf{y}(t)\end{aligned} \tag{17}$$

$$\begin{aligned}\breve{y}^*(t+\tau) &\approx y^{\alpha *}(t) + \tau y^{\alpha *(1)}(t) + \cdots + \frac{\tau^{3+r}}{(3+r)!} y^{\alpha *(3+r)}(t) \\ &= \Im(\tau)\mathbf{y}^*(t)\end{aligned} \tag{18}$$

where $\Im(\tau) = [1 \tau \ldots \frac{\tau^{3+r}}{(3+r)!}]$, $\mathbf{y}(t) = [y^{\alpha}(t) y^{\alpha(1)}(t) \ldots y^{\alpha(3+r)}(t)]^T$, $\mathbf{y}^*(t) = [y^{\alpha *}(t)\ y^{\alpha *(1)}(t)\ \ldots\ y^{\alpha *(3+r)}(t)]^T$, and r is the control order with the definition mentioned in [31]. In this article, r is selected as 1 for facilitating the practical implementation.

Rewriting the cost function (16) in terms of (17) and (18) yields

$$J = \frac{1}{2}\int_0^{T_P} [\mathbf{y}^*(t) - \mathbf{y}(t)]^T \Im(\tau)^T \Im(\tau)[\mathbf{y}^*(t) - \mathbf{y}(t)]\, d\tau$$
$$= \frac{1}{2}[\mathbf{y}^*(t) - \mathbf{y}(t)]^T \bar{\Im}\,[\mathbf{y}^*(t) - \mathbf{y}(t)] \tag{19}$$

where $\bar{\Im} = \int_0^{T_P} \Im^T(\tau)\Im(\tau)d\tau$

$$= \begin{bmatrix} 1 & T_P & {T_P}^2/2 & {T_P}^3/6 & {T_P}^4/24 \\ T_P & {T_P}^2 & {T_P}^3/2 & {T_P}^4/6 & {T_P}^5/24 \\ {T_P}^2/2 & {T_P}^3/2 & {T_P}^4/4 & {T_P}^5/12 & {T_P}^6/48 \\ {T_P}^3/6 & {T_P}^4/6 & {T_P}^5/12 & {T_P}^6/36 & {T_P}^7/144 \\ {T_P}^4/24 & {T_P}^5/24 & {T_P}^6/48 & {T_P}^7/144 & {T_P}^8/576 \end{bmatrix}.$$

The matrix $\bar{\Im}$ is divided into the submatrices as

$$\bar{\Im} = \begin{bmatrix} \bar{\Im}_{33} & \bar{\Im}_{31} \\ \bar{\Im}_{31}^T & \bar{\Im}_{11} \end{bmatrix} \tag{20}$$

where

$$\bar{\Im}_{33} = \begin{bmatrix} 1 & T_P & {T_P}^2/2 \\ T_P & {T_P}^2 & {T_P}^3/2 \\ {T_P}^2/2 & {T_P}^3/2 & {T_P}^4/4 \end{bmatrix}, \quad \bar{\Im}_{31} = \begin{bmatrix} {T_P}^3/6 & {T_P}^4/24 \\ {T_P}^4/6 & {T_P}^5/24 \\ {T_P}^5/12 & {T_P}^6/48 \end{bmatrix}$$
$$\bar{\Im}_{11} = \begin{bmatrix} {T_P}^6/36 & {T_P}^7/144 \\ {T_P}^7/144 & {T_P}^8/576 \end{bmatrix}.$$

The tracking error $[\mathbf{y}^*(t) - \mathbf{y}(t)]$ is expressed as

$$[\mathbf{y}^*(t) - \mathbf{y}(t)] = \begin{bmatrix} y^{\alpha*}(t) - y^{\alpha}(t) \\ y^{\alpha*(1)}(t) - y^{\alpha(1)}(t) \\ y^{\alpha*(2)}(t) - y^{\alpha(2)}(t) \\ y^{\alpha*(3)}(t) - b_0 v_i^{\alpha}(t) - \bar{g}^{\alpha} \\ y^{\alpha*(4)}(t) - b_0 v_i^{\alpha(1)}(t) - \bar{g}^{\alpha(1)} \end{bmatrix}$$
$$= \mathbf{M} - \begin{bmatrix} \mathbf{0}_{3\times 1} \\ \mathbf{N}(\mathbf{v}_i^{\alpha}) \end{bmatrix} \tag{21}$$

$$\mathbf{M} = \begin{bmatrix} y^{\alpha*}(t) - y^{\alpha}(t) \\ y^{\alpha*(1)}(t) - y^{\alpha(1)}(t) \\ y^{\alpha*(2)}(t) - y^{\alpha(2)}(t) \\ y^{\alpha*(3)}(t) \\ y^{\alpha*(4)}(t) \end{bmatrix}, \quad \mathbf{N}(\mathbf{v}_i^{\alpha})$$
$$= \begin{bmatrix} b_o v_i^{\alpha}(t) + \bar{g}^{\alpha}(t) \\ b_o v_i^{\alpha(1)}(t) + \bar{g}^{\alpha(1)}(t) \end{bmatrix}, \quad \mathbf{v}_i^{\alpha}$$
$$= \begin{bmatrix} v_i^{\alpha}(t) \\ v_i^{\alpha(1)}(t) \end{bmatrix}, \bar{g}^{\alpha} = g^{\alpha} + \eta x_2^{\alpha}.$$

Substituting (20) and (21) into (19), the cost function J is expressed as

$$J = \frac{1}{2}\left[\mathbf{M} - \begin{bmatrix} \mathbf{0}_{3\times 1} \\ \mathbf{N}(\mathbf{v}_i^{\alpha}) \end{bmatrix}\right]^T \begin{bmatrix} \bar{\Im}_{33} & \bar{\Im}_{31} \\ \bar{\Im}_{31}^T & \bar{\Im}_{11} \end{bmatrix} \left[\mathbf{M} - \begin{bmatrix} \mathbf{0}_{3\times 1} \\ \mathbf{N}(\mathbf{v}_i^{\alpha}) \end{bmatrix}\right]$$
$$\text{or } J = \frac{1}{2}\mathbf{M}^T \begin{bmatrix} \bar{\Im}_{33} & \bar{\Im}_{31} \\ \bar{\Im}_{31}^T & \bar{\Im}_{11} \end{bmatrix} \mathbf{M} - \begin{bmatrix} \mathbf{0}_{3\times 1} \\ \mathbf{N}(\mathbf{v}_i^{\alpha}) \end{bmatrix}^T \begin{bmatrix} \bar{\Im}_{33} & \bar{\Im}_{31} \\ \bar{\Im}_{31}^T & \bar{\Im}_{11} \end{bmatrix} \mathbf{M}$$
$$+\frac{1}{2}\mathbf{N}(\mathbf{v}_i^{\alpha})^T \bar{\Im}_{11} \mathbf{N}(\mathbf{v}_i^{\alpha}). \tag{22}$$

Taking the partial derivative of J in (22) with respect to $\mathbf{v}_i^{\alpha}$ yields

$$\frac{\partial J}{\partial \mathbf{v}_i} = -\left(\frac{\partial \mathbf{N}(\mathbf{v}_i)}{\partial \mathbf{v}_i}\right)^T \left[\, \bar{\Im}_{31}^T \; \bar{\Im}_{11} \,\right] \mathbf{M}$$
$$+ \left(\frac{\partial \mathbf{N}(\mathbf{v}_i)}{\partial \mathbf{v}_i}\right)^T \bar{\Im}_{11} \mathbf{N}(\mathbf{v}_i^{\alpha}). \tag{23}$$

Letting $\frac{\partial J}{\partial \mathbf{v}_i^{\alpha}} = 0$, the optimized control input $\mathbf{v}_i^{\alpha*}(t)$ is obtained as

$$\mathbf{N}(\mathbf{v}_i^{\alpha*}) = \left[\, \bar{\Im}_{11}^{-1}\bar{\Im}_{31}^T \; \mathbf{I}_{2\times 2} \,\right] \mathbf{M} \tag{24}$$

in which $\mathbf{I}_{2\times 2}$ is a 2×2 identity matrix. Considering the expression of $\mathbf{N}(\mathbf{v}_i^{\alpha*})$ in (21), the first row of (24) can be written as

$$b_0 v_i^{\alpha*}(t) + \bar{g}^{\alpha} = \left[\, k_1 \; k_2 \; k_3 \; 1 \; 0 \,\right] \mathbf{M} \tag{25}$$

with $[\, k_1 \; k_2 \; k_3 \,] = [\, \frac{336}{5T_P^3} \; \frac{168}{5T_P^2} \; \frac{8}{T_P} \,]$ is the first row of matrix $\bar{\Im}_{11}^{-1}\bar{\Im}_{31}^T$.

As a result, the optimal control input of the GCI is expressed as follows:

$$v_i^{\alpha*}(t) = \frac{1}{b_o}[k_1(y^{\alpha*}(t) - y^{\alpha}(t)) + k_2(y^{\alpha*(1)}(t) - y^{\alpha(1)}(t))$$
$$+k_3(y^{\alpha*(2)}(t) - y^{\alpha(2)}(t)) + y^{\alpha*(3)}(t) - \bar{g}^{\alpha}(t)]. \tag{26}$$

It is worth to note that, in practical implementation, $y^{\alpha}(t)$, $y^{\alpha(1)}(t)$, $y^{\alpha(2)}(t)$, and $\bar{g}^{\alpha}$ are replaced by their estimates generated by the observer in (9) as follows:

$$v_i^{\alpha*}(t) = \frac{1}{b_o}[k_1(y^{\alpha*}(t) - \hat{x}_1^{\alpha}(t)) + k_2(y^{\alpha*(1)}(t) - \hat{x}_2^{\alpha}(t))$$
$$+k_3(y^{\alpha*(2)}(t) - \hat{x}_3^{\alpha}(t)) + y^{\alpha*(3)}(t) - \eta\hat{x}_2^{\alpha}(t) - \hat{x}_4^{\alpha}(t)]. \tag{27}$$

Since the prediction time T_P is a positive constant, the characteristic equation of the proposed controller represented as

$$P(s) = s^3 + k_3 s^2 + k_2 s + k_1 \tag{28}$$

is always Hurwitz stable. Thus, the given optimal control input in (27) ensures that the output state trajectory is driven to track the reference asymptotically.

It is clearly shown that the controller gains are obtained as a function of the predictive period T_P. Unlike the linear quadratic regulator-based approach that requires to tune multiple design factors, the optimal gain selection in (25) is determined based on only one design parameter T_P, which further reduces the laborious work.

B. Robustness and Stability Analysis

The ARDC structure can be established as a 2-DOF form to analyze the robustness and stability of the system [37], [38]. The proposed state-space ADRC-based controller comprised of the discrete current-type RESO and linear state feedback controller

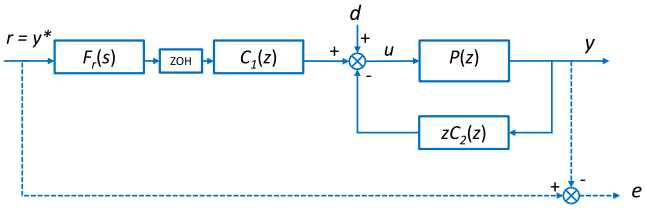

Fig. 3. Equivalent framework of ADRC in view of the 2-DOF form.

is expressed as

$$\hat{\mathbf{x}}(k+1) = [\mathbf{\Phi} - \mathbf{LH\Phi}]\hat{\mathbf{x}}(k) + [\mathbf{\Gamma} - \mathbf{LH\Gamma}]u(k) + \mathbf{L}y^{\alpha}(k+1) \tag{29}$$

$$u(k) = \mathbf{K}[\mathbf{r}(k) - \hat{\mathbf{x}}(k)] - \mathbf{G}\hat{\mathbf{x}}(k) \tag{30}$$

where $\mathbf{K} = \frac{1}{b_o}[k_1\ k_2\ k_3\ 1\ 0]$, $\mathbf{G} = \frac{1}{b_o}[0\ \eta\ 0\ 0\ 0]$, $u(k) = v_i^{\alpha}(k)$

$$\mathbf{r}(k) = \left[y^{\alpha *}(k)\ y^{\alpha *(1)}(k)\ y^{\alpha *(2)}(k)\ y^{\alpha *(3)}(k)\ 0\right]^{T}.$$

Taking the *Z*-transform into (29) and (30) yields

$$z\hat{\mathbf{x}}(z) = [\mathbf{\Phi} - \mathbf{LH\Phi}]\hat{\mathbf{x}}(z) + [\mathbf{\Gamma} - \mathbf{LH\Gamma}]u(z) + \mathbf{L}zy^{\alpha}(z) \tag{31}$$

$$u(z) = \mathbf{K}[\mathbf{r}(z) - \hat{\mathbf{x}}(z)] - \mathbf{G}\hat{\mathbf{x}}(z) = \mathbf{K}\mathbf{r}(z) - (\mathbf{K}+\mathbf{G})\hat{\mathbf{x}}(z) \tag{32}$$

where $\mathbf{r}(z) = Z\{[1\ s\ s^2\ s^3\ 0]^T R(s)\}$ and $R(s)$ is the Laplace transform of the current reference $y^{\alpha *}$. By substituting $u(z)$ in (32) into (31), $\hat{\mathbf{x}}(z)$ is solved as

Then, substituting (33) as shown at bottom of this page into (32) yields $u(z)$ into two parts according to the reference signal $r(z)$ and the measured output $y(z)$ as

$$u(z) = C_1(z)F_r(z) - C_2(z)zy^{\alpha}(z) \tag{34}$$

where $F_r(z) = Z\{\mathbf{K}\mathbf{r}(s)\}$

$$C_1(z) = 1 - (\mathbf{K}+\mathbf{G})[z\mathbf{I} - [\mathbf{\Phi} - \mathbf{LH\Phi}] + [\mathbf{\Gamma} - \mathbf{LH\Gamma}](\mathbf{K}+\mathbf{G})]^{-1}[\mathbf{\Gamma} - \mathbf{LH\Gamma}]$$

$$C_2(z) = (\mathbf{K}+\mathbf{G})[z\mathbf{I} - [\mathbf{\Phi} - \mathbf{LH\Phi}] + [\mathbf{\Gamma} - \mathbf{LH\Gamma}](\mathbf{K}+\mathbf{G})]^{-1}\mathbf{L}.$$

The structure of the proposed controller can be depicted in Fig. 3. The numerical simulations are carried out in the frequency domain to study the robustness and stability of the proposed ADRC-based current controller. It is observed from the system model (8) that the parameter variations in the filter inductances L_1 and L_2, and the grid impedance L_g caused by weak grid have a similar effect to the system behavior; therefore, the analysis

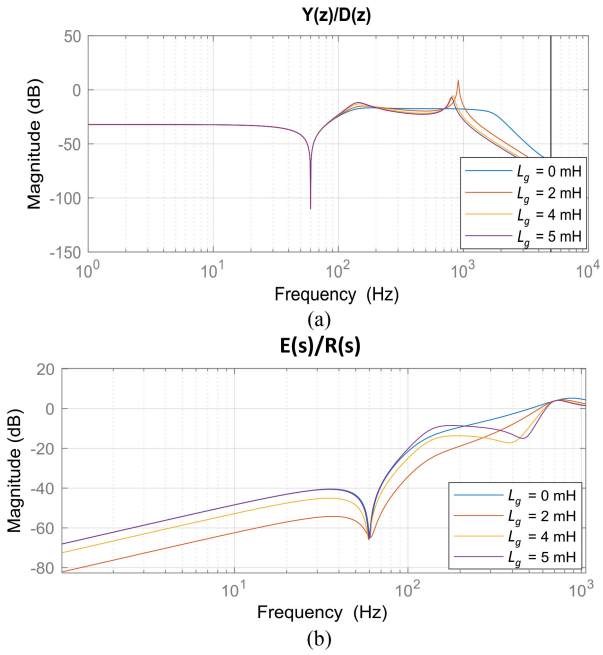

Fig. 4. Frequency response of the transfer functions under grid inductor variations. (a) $G_{yd}(z)$. (b) $G_{er}(s)$.

for only L_g variations is considered together with the effect of the filter capacitor C_f variation. To conduct the robustness and stability analysis, in this section, the *LCL* filter parameters are designed for GCI in the low-frequency region, where L_1, L_2, and C_f are chosen as 1.7 mH, 1 mH, and 30 μF, respectively. The controller parameters for the optimized ADRC control law and the observer gains are set as

$k_1 = 4.779 \times 10^{11}$, $k_2 = 1.243 \times 10^{8}$, $k_3 = 1.539 \times 10^{4}$

$l_1 = 0.865$, $l_2 = 6.489 \times 10^{3}$, $l_3 = 2.5 \times 10^{7}$, $l_4 = 5.019 \times 10^{10}$ $l_5 = -4.665 \times 10^{10}$.

To verify the disturbance rejection and tracking performance of the proposed current controller, the transfer function from the disturbance $D(z)$ to the system output $Y(z)$ and the transfer function from reference $R(s)$ to tracking error $E(s)$ are obtained as follows:

$$G_{dy}(z) = \frac{Y(z)}{D(z)} \tag{35}$$

$$G_{er}(s) = \frac{E(s)}{R(s)} = 1 - \frac{Y(s)}{R(s)}. \tag{36}$$

Accordingly, the frequency responses of $G_{dy}(z)$ and $G_{er}(s)$ are presented in Fig. 4(a) and (b), respectively, under the grid inductance variation from stiff grid ($L_g = 0$ mH) to weak grid ($L_g = 5$ mH). Obviously, the proposed ADRC combined with the

$$\hat{\mathbf{x}}(z) = [z\mathbf{I} - [\mathbf{\Phi} - \mathbf{LH\Phi}] + [\mathbf{\Gamma} - \mathbf{LH\Gamma}](\mathbf{K}+\mathbf{G})]^{-1}[\mathbf{\Gamma} - \mathbf{LH\Gamma}]\ \mathbf{K}\mathbf{r}(z) + [z\mathbf{I} - [\mathbf{\Phi} - \mathbf{LH\Phi}] + [\mathbf{\Gamma} - \mathbf{LH\Gamma}](\mathbf{K}+\mathbf{G})]^{-1}\mathbf{L}zy^{\alpha}(z) \tag{33}$$

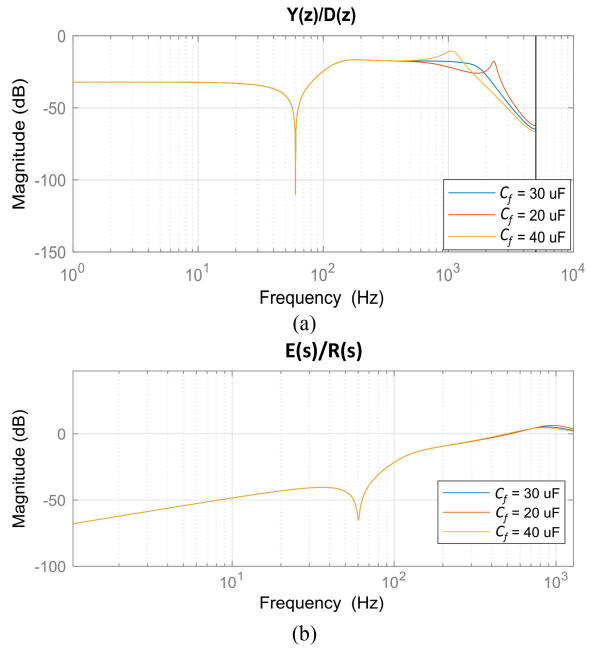

Fig. 5. Frequency response of the transfer functions under filter capacitor variations. (a) $G_{yd}(z)$. (b) $G_{er}(s)$.

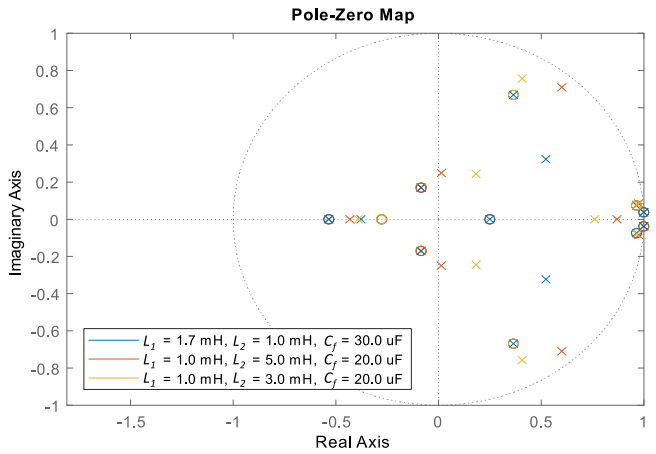

Fig. 6. Pole-zero map of the ADRC-based current controller under parameter variations.

RESO provides complete disturbance rejection and ideal tracking performance at the fundamental frequency ω with significant low gain magnitude in $G_{dy}(z)$ and $G_{er}(s)$ even under the weak grid and stiff grid. In case of the filter capacitor deviation from 20 to 40 μF in Fig. 5, the frequency responses also reveal that the proposed controller is quite immune to the capacitor variations as expected.

The system stability is investigated with the pole-zero plot analysis under three different sets of *LCL* filter parameters. By using the closed-loop transfer function from the reference $R(z)$ to the output $Y(z)$ inferred from Fig. 3, the closed-loop poles' locations are examined to verify the stability of the proposed scheme in specific cases. Fig. 6 shows the locations of poles and zeros for three different cases. The first case corresponds to the *LCL* filter parameters having the nominal values. In the second case, L_1 varies by -40%, L_2 varies by 500%, and C_f varies by -33% from their nominal values. Finally, the last case shows the results for L_1 variation of -40%, L_2 variation of 300%, and C_f variation of -33% from their nominal values. Obviously, the locations of the closed-loop poles in those cases are still maintained in the unit circle, which demonstrates the stability of the proposed control scheme under severe filter parametric variations. Furthermore, the experimental results in Section V are also presented to evaluate the robustness and stability of the proposed scheme.

C. Frequency Adaptive Harmonic Compensators

In the literature [15], [20], the effectiveness of the resonant controller designed in the discrete-time domain has been demonstrated to reject selected harmonics with the frequency adaptive capability. In the proposed scheme, the resonant controller in the z-domain given by (37) is integrated with the ADRC-based current controller to suppress the distorted harmonics from the grid as follows:

$$\mathrm{PR}_h(z) = \frac{z^2 - \left(2 - \frac{(h\omega T_s)^2}{2} + \frac{(h\omega T_s)^4}{24}\right) z + \left(1 - \frac{(h\omega T_s)^2}{2} + \frac{(h\omega T_s)^4}{24}\right)}{z^2 - 2\cos(h\omega T_s) z + 1} \tag{37}$$

where h is the harmonic order. Based on (37), the output of the resonant controller is obtained as

$$v_{\mathrm{PR}}(t) = Z^{-1}\left\{\sum\nolimits_{h=5,7,11\ldots} g_h \mathrm{PR}_h(z)\left[R(z) - Y(z)\right]\right\} \tag{38}$$

where g_h is the control gain. Consequently, this output is added with the optimized ADRC-based control input in (27) to form the final control law as

$$v_i^{\alpha}(t) = v_i^{\alpha *}(t) + v_{\mathrm{PR}}(t). \tag{39}$$

The resonant control gains are tuned by an iterative process for experimental verification to achieve the best performance.

V. Simulation and Experimental Results

For the purpose of validating the effectiveness and feasibility of the proposed current controller, both the simulation and experimental tests are carried out by using the PSIM software and the hardware prototype with the construction following Figs. 1 and 7. In the experimental platform in Fig. 7, the ac power source (PACIFIC 320-ASX) is utilized to emulate the unity grid in both ideal and nonideal conditions. A digital signal processor (DSP) TMS320F28335 control board is used to execute the proposed algorithm in real time with the measured inputs from the dc-link voltage and grid-side current sensors. It is worth to note that, the grid voltage sensors are still installed for the comparison purpose only, without the utilization in the control algorithm. Two *LCL* filter sets designed in the high region with $C_f = 4.5$ μF and low region with $C_f = 30$ μF (i.e., the *LCL* resonance frequency is greater and less than one-sixth sampling frequency, respectively) are used in the experimental tests to demonstrate

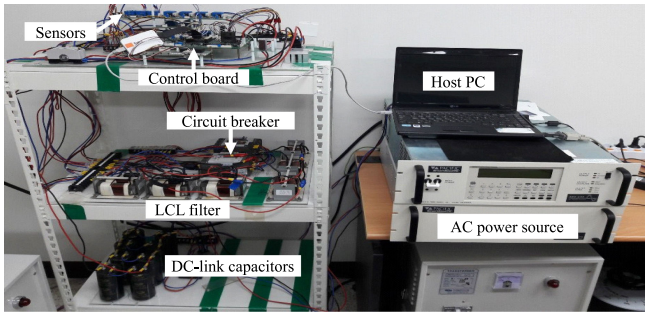

Fig. 7. Experimental setup.

TABLE I
SYSTEM PARAMETERS OF GCI

Symbol	Parameter	Value	Units
L_1	inverter-side filter inductor	1.7	mH
L_2	grid-side filter inductor	1.0	mH
L_g	grid inductance	0.0, 1.0, 3.0, 5.0	mH
C_f	filter capacitor	30.0/4.5	μF
V_{DC}	DC link voltage	420	V
v_d	grid voltage (line-to-line rms)	220	V
f_g	grid frequency	60/50	Hz
f_{sw}	switching frequency	10	kHz
f_{samp}	sampling frequency	10	kHz

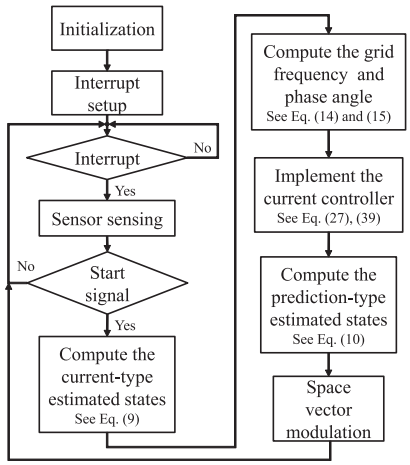

Fig. 8. Flowchart of the proposed voltage sensorless control scheme.

the applicability and flexibility of the control design process. The detailed system parameters are listed in Table I. The control flow chart of the proposed sensorless current control, which is implemented in the simulation and experiment, is presented in Fig. 8.

A. Simulation Results

The objective of this simulation is to verify the tracking performance of output currents from the proposed ADRC grid voltage sensorless controller under adverse and perturbed conditions. First, the grid environment containing harmonic distortion at 5th and 7th with the magnitude of 5% of fundamental grid component and 11th with the magnitude of 3% of fundamental grid component is represented in Fig. 9(a), which results in

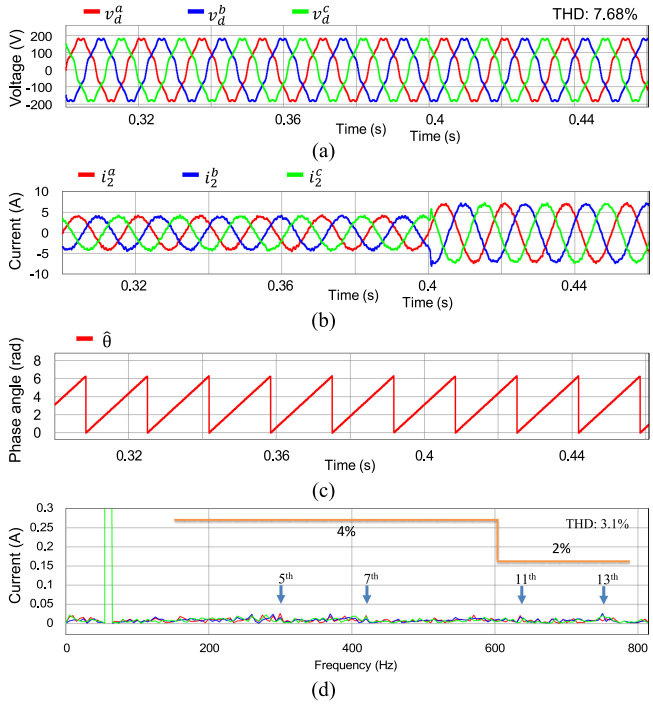

Fig. 9. Simulation of current response under distorted grid voltages under the nominal *LCL* filter set: $L_1 = 1.7$ mH, $C_f = 30$ μF, and $L_2 = 1$ mH. (a) Three-phase grid voltages. (b) Three-phase grid currents under current reference change from 4 to 7 A. (c) Estimated grid phase angle. (d) FFT result of the three-phase grid currents.

the voltage total harmonic distortion (THD) of 7.68%. The dynamic performance of the grid-injected phase currents under the nominal *LCL* filter set ($L_1 = 1.7$ mH, $L_2 = 1.0$ mH, and $C_f = 30.0$ μF) is shown in Fig. 9(b) when the reference has a step jump from 4 to 7 A at 0.4 s. A fast transient response without overshoot can be observed. Also, quite sinusoidal waveforms and good synchronization, as shown in Fig. 9(b) and (c), are achieved regardless of the influence from the distorted grid conditions, resulting in a low current THD value of 3.1%. The current fast Fourier transform (FFT) spectrum in Fig. 9(d) also confirms the negligible magnitude of current at the contaminated harmonic orders from the grid.

The next test is conducted to verify the robustness of the proposed strategy against *LCL* parametric variations and severe disturbances from the main grid. In particular, the *LCL* filter setup is varied by −40% in L_1 and by −33% in C_f. In addition, different variations in three phases of the grid-side inductors are applied as L_2 in phase a (denoted as L_{2a}) increases to five times the nominal value, while the L_2 in phases b and c (denoted as L_{2b} and L_{2c}) is set as three times the nominal value. As an external disturbance, the grid includes unbalanced and distorted grid voltages as well as the grid frequency jump in a wide range of 10 Hz. It can be seen that the test condition simulates the worst case of parametric variation and grid condition to verify the performance of the proposed scheme. As shown in Fig. 10(a), phase a grid voltage is dropped by 30% comparing with the nominal voltage value, and all phase voltages contain the same harmonic levels as Fig. 9. Moreover, the grid frequency jumps

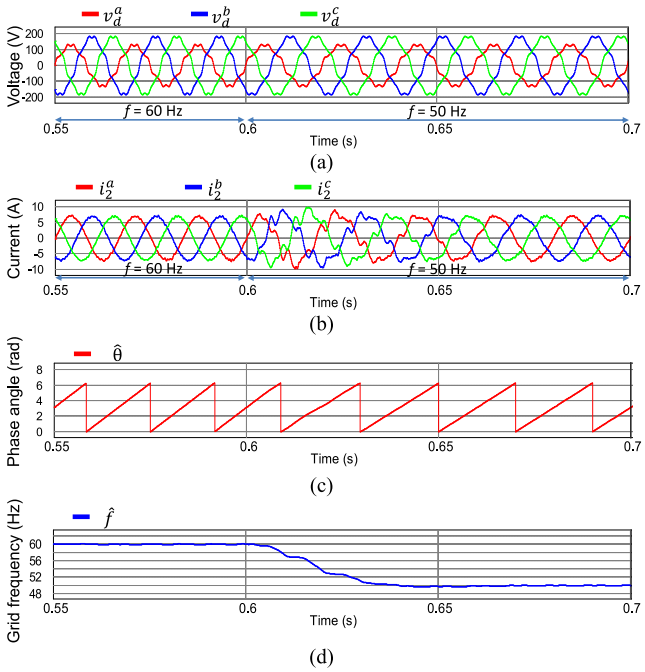

Fig. 10. Simulation of current response under distorted and unbalanced grid voltages with the grid frequency variation from 60 to 50 Hz at 0.6 s, and the *LCL* parameter variations as: $L_1 = 1$ mH, $C_f = 20$ μF, $L_{2a} = 5$ mH, $L_{2b} = 3$ mH, and $L_{2c} = 3$ mH. (a) Three-phase grid voltages. (b) Three-phase grid currents. (c) Estimated grid phase angle. (d) Estimated grid frequency.

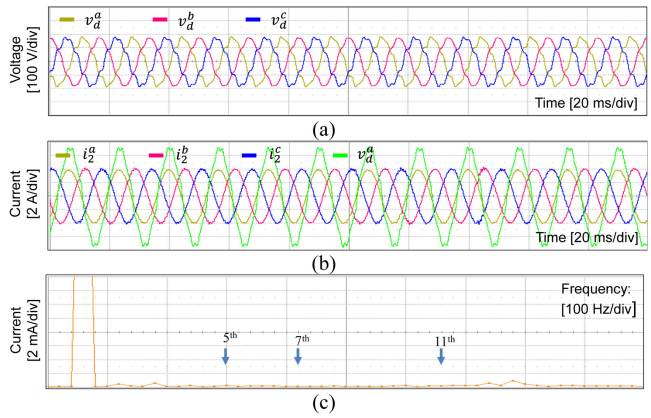

Fig. 11. Experimental results of current response under distorted grid voltages with $L_1 = 1.7$ mH, $L_2 = 1$ mH, and $C_f = 30$ μF. (a) Three-phase grid voltages. (b) Steady-state three-phase grid currents. (c) FFT result of phase *a* current.

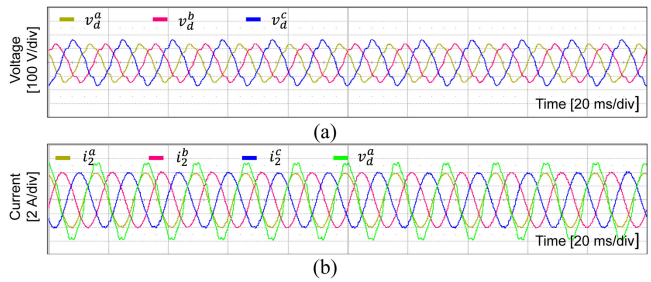

Fig. 12. Experimental results of current response under distorted and unbalanced grid voltages with $L_1 = 1$ mH, $L_2 = 5$ mH, and $C_f = 20$ μF. (a) Three-phase grid voltages. (b) Steady-state three-phase grid currents.

suddenly from 60 to 50 Hz at 0.6 s. The grid-current responses are found in Fig. 10(b) in which phase currents reach the steady state with quite sinusoidal waveforms and zero tracking error at the grid frequency of 60 Hz. At 0.6 s, the grid frequency jump causes a transient period in the grid-injected currents, which lasts around 50 ms. However, it can be observed that the overshoot currents are just a maximum of 40% and the currents quickly converge to stable sinusoidal waveforms with a new grid frequency of 50 Hz. Evidently, the proposed strategy well damps the inherent *LCL* resonance phenomenon as well as attenuates all the severe influences from internal and external disturbances to ensure a reliable operation.

The superior current responses are achieved due to the disturbance estimation and rejection capability of the proposed ADRC-based control combining the harmonic compensation from resonant controllers. Furthermore, by means of the high-performance grid frequency and phase angle estimator, as well as the frequency adaptability feature enabled in the RESO and resonant controllers, the synchronization between the inverter and main grid is guaranteed. As a result, optimal performance is ensured even with only the grid-current sensors measurement.

B. Experimental Results

1) LCL Filter in Low Region: Similar to the simulation setup, the *LCL* filter resonance frequency is designed in the low region by choosing C_f with 30 μF. The first experiment is conducted under distorted grid condition, as shown in Fig. 11(a), with the harmonic contamination level equal to the simulation. The peak value of the grid-injected current reference is selected to 4 A. The steady-state tracking performance of the grid-current controlled by the proposed ADRC-based strategy is shown in Fig. 11(b). It can be observed that good sinusoidal current waveforms are obtained without the effect of distorted harmonics. To assess the grid-injected current quality, phase difference between the output current and measured grid voltage in phase *a* and the current FFT spectrum are also shown in Fig. 11(b) and (c), respectively. The phase *a* current FFT result shows unnoticeable magnitudes at low-order harmonics, which well agrees with the simulation result in Fig. 9(d). Moreover, the appropriate match between the phase angles of current and grid voltage in Fig. 11(b) demonstrates the effectiveness of the synchronization technique even without voltage sensor installation.

In the next test, the robustness of the proposed current controller against the severe parametric mismatches and adverse grid conditions is evaluated. Particularly, the three-phase inverter-side inductor and capacitor values are reduced to 1 mH and 20 μF, respectively, while the grid-side inductors vary in a wide range up to 5 mH to demonstrate the impact in a weak grid. At the same time, the background grid voltages have not only distorted harmonics but also unbalanced condition with both phase *a* and phase *b* voltage drop compared with the nominal voltage value, as shown in Fig. 12(a). Fig. 12(b) depicts the steady-state performance of the output currents controlled by the proposed scheme. As expected, the phase currents are kept at

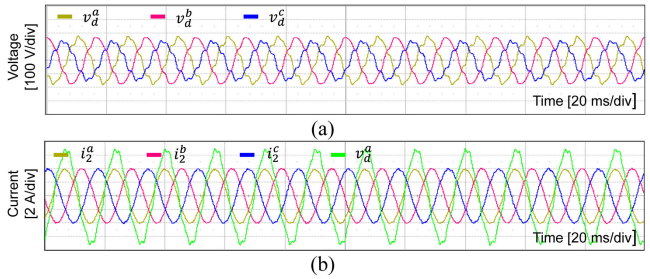

Fig. 13. Experimental results of current response under distorted and unbalanced grid voltages with $L_1 = 1$ mH, $L_{2a} = 5$ mH, $L_{2b} = 3$ mH, $L_{2c} = 3$ mH, and $C_f = 20$ μF. (a) Three-phase grid voltages. (b) Steady-state three-phase grid currents.

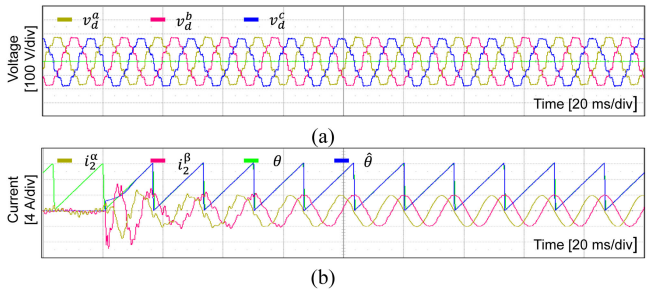

Fig. 14. Experimental results of grid currents at start-up instant and three-phase grid voltage sag under distorted grid with $L_1 = 1.7$ mH, $L_2 = 1$ mH, and $C_f = 4.5$ μF. (a) Three-phase distorted grid voltages. (b) Grid-current in the stationary frame and comparison between $\hat{\theta}$ and θ at the start-up instant.

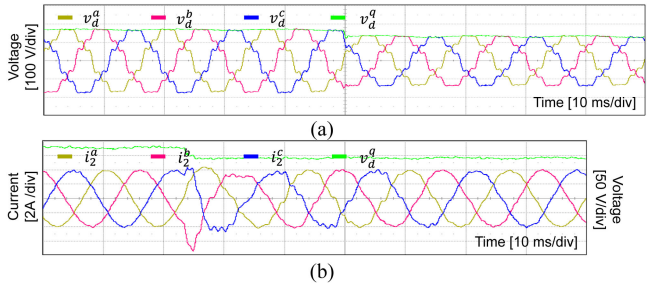

Fig. 15. Experimental results of grid currents under three-phase distorted grid voltage sag from 180 to 140 V with $L_1 = 1.7$ mH, $L_2 = 1$ mH, and $C_f = 4.5$ μF. (a) Three-phase distorted grid voltages. (b) Three-phase grid-side current and the q-axis grid voltage.

balanced sinusoidal waveforms. The experimental verifications in terms of the effective damping and high robustness operation confirm the notable properties of the proposed control strategy. In particular, the influences of unbalanced grid voltages and parameter mismatch in the *LCL* filter are dealt with as a lumped sinusoidal disturbance. Since the proposed RESO is able to provide estimations for system states and disturbance, it facilitates the resonant-ADRC current controller to achieve the optimized tracking performance. Furthermore, the proposed grid frequency and phase angle estimations are immune to the effects of unbalanced and distorted grid conditions; therefore, the high-quality injected power is guaranteed.

One of the prominent characteristics of the proposed current control brought by the ADRC concept is that the filter parameters in three phases are not required to be exactly the same. It well reflects the condition in control practice, especially when the manufacturing tolerance is common in industrial circuit components. To verify the system performance under this situation in the experiment, the grid-side inductors are selected as the same value as the simulation in Fig. 10 in which the grid inductor in phase a is 5 mH, while those in other phases are 3 mH. In this experiment, the grid phase currents in Fig. 13(b) also show satisfactory waveforms under distorted and unbalanced voltages, as depicted in Fig. 13(a), which is well matched to the simulation in Fig. 10(b). The stable current responses in both simulation and experiment under such severe parameter variation effectively verify the theoretical stability analysis in Section IV.

2) LCL Filter in High Region: The dynamic performance of the proposed strategy is further tested experimentally for the inverter system with an *LCL* filter designed in the high region ($C_f = 4.5$ μF).

Fig. 14 shows the experimental results of start-up instant under distorted grid with $L_1 = 1.7$ mH, $L_2 = 1$ mH, and $C_f = 4.5$ μF. Fig. 14(b) shows the start-up instant of the proposed current controller under distorted grid voltages in Fig. 14(a) in which the grid voltages contain distorted harmonic at 5th, 7th, 11th, and 13th with a magnitude of 5% of fundamental grid component. In Fig. 14(b), the grid currents in the stationary frame are shown together with the estimated grid phase angle $\hat{\theta}$ from the proposed estimator and the phase angle θ obtained for the synchronous reference frame phase-locked loop (SRF-PLL) with the measured grid voltages from sensors. Even though the proposed scheme does not apply any extra start-up process to estimate the actual grid information, the sensorless operation still can be started softly and stably with rapidly damped overshoot currents. Also, the estimated grid phase angle well tracks the actual one during less than 10 ms.

Fig. 15 shows the grid-current responses under sudden three-phase distorted grid voltages sag from 180 to 140 V, as displayed in Fig. 15(a). At the voltage sag instant, the grid currents encounter a short transient period with an overshoot of 7 A, then the output currents are recovered back to the steady state in a few cycles, as presented in Fig. 15(b).

In the next tests, the current reference step change and the grid frequency variation in a range of 10 Hz are considered to verify the dynamic response of the proposed current control scheme. The current responses with the nominal filter parameters are evaluated first in Fig. 16 in which the grid voltages contain distorted harmonic at 5th, 7th, 11th, and 13th, together with voltage drops in phases a and b, as shown in Fig. 16(a). It can be observed in Fig. 16(b) that good sinusoidal grid currents under steady-state condition and a fast reference tracking under current reference change from 2 to 4 A are achieved.

The experimental results of current response under distorted and unbalanced grid voltages and the grid frequency variation are represented in Fig. 17. Under rapid grid frequency variation from 60 to 50 Hz in Fig. 17(a), an oscillation of the grid-side currents is observed during the transient time in Fig. 17(b). However, the estimated frequency $\hat{f}$ and phase angle $\hat{\theta}$ by the proposed estimator well converge to the actual f and θ within only one and

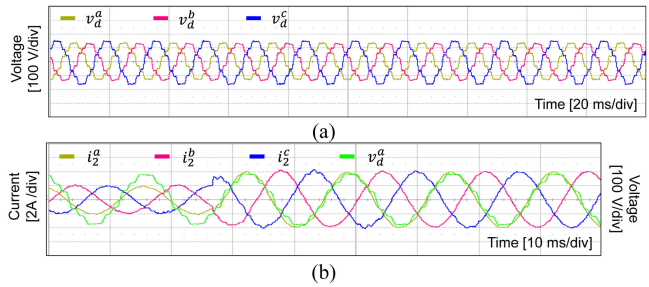

Fig. 16. Experimental results of current response under distorted and unbalanced grid voltages with $L_1 = 1.7$ mH, $L_2 = 1$ mH, and $C_f = 4.5$ μF. (a) Three-phase grid voltages. (b) Three-phase grid currents under the current reference change.

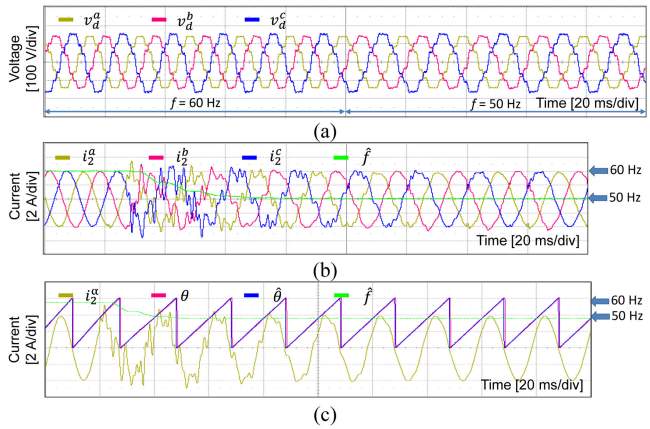

Fig. 17. Experimental results of current response under distorted unbalanced grid voltages and grid frequency variation from 60 to 50 Hz with $L_1 = 1.7$ mH, $L_2 = 1$ mH, and $C_f = 4.5$ μF. (a) Three-phase grid voltages. (b) Three-phase grid currents (c) α-axis grid current, estimated grid frequency $\hat{f}$, and comparison between $\hat{\theta}$ and θ.

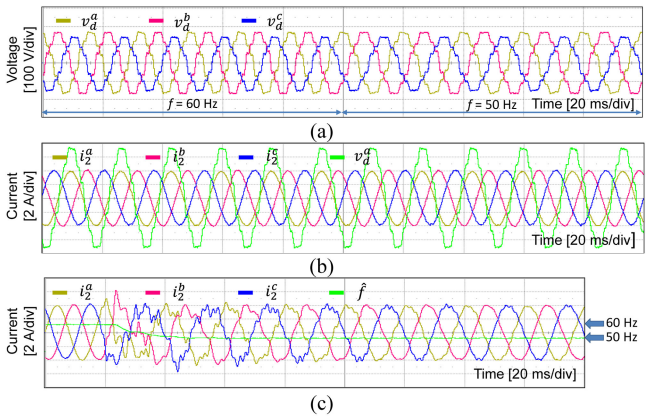

Fig. 18. Experimental results of current response under distorted and unbalanced grid voltages with $L_1 = 3$ mH, $L_2 = 5$ mH, $C_f = 3$ μF, and grid frequency change from 60 to 50 Hz. (a) Three-phase grid voltages. (b) Steady-state three-phase grid currents at 60 Hz. (c) Three-phase grid currents under grid frequency variation from 60 to 50 Hz.

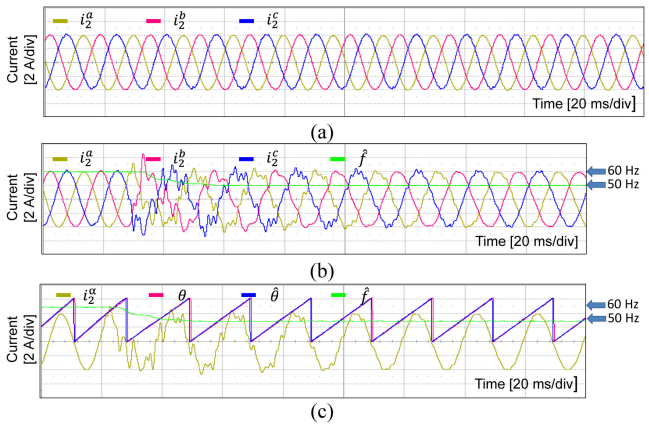

Fig. 19. Experimental results of current response under distorted and unbalanced grid voltages with $L_1 = 3$ mH, $L_{2a} = 5$ mH, $L_{2b} = 3$ mH, $L_{2c} = 1$ mH, and $C_f = 3$ μF. (a) Steady-state three-phase grid currents at 60 Hz. (b) Three-phase grid currents under grid frequency variation from 60 to 50 Hz. (c) α-axis grid current, estimated grid frequency $\hat{f}$, and comparison between $\hat{\theta}$ and θ.

half fundamental period, as shown in Fig. 17(c). Accordingly, the grid currents are successfully stabilized within four fundamental periods. This overshoot phenomenon of 7 A, which is within the range of system protection, and the acceptable transient time well demonstrate the dynamic performance of the synchronization technique and the frequency adaptability of the proposed grid voltage sensorless current controller.

Next, the proposed controller is experimentally tested under the variations of *LCL* parameters from their nominal values as follows: the inverter-side inductors L_1 and the grid-side inductors L_2 are increased to three times and five times, respectively, while the filter capacitors are decreased to two-third times of the nominal quantities. The background grid environment still contains both distorted unbalanced disturbances and grid frequency variation, as shown in Fig. 18(a). The corresponding results of grid-side currents are presented in Fig. 18(b). Obviously, the grid-injected currents show stable and balanced waveforms in the steady state with good tracking of current phase angle to the grid phase angle, which indicates that the synchronization task of the controller is unaffected by the adverse grid condition. The dynamic performance of the controller is also tested under the grid frequency variation in a range of 10 Hz, as given in Fig. 18(c). It is noticed that the similarity between the current responses in Fig. 17(b) and 18(c) is observed. In both figures, the total transient period lasts around four grid fundamental periods and estimated grid frequency rapidly tracks the actual quantity. These responses further validate the capability of the proposed controller in terms of immunity to the internal disturbances caused by parametric uncertainties and external disturbances from the grid environment.

Finally, the condition of unbalanced grid inductances in three phases is considered as $L_{2a} = 1$ mH, $L_{2b} = 3$ mH, and $L_{2c} = 5$ mH, whereas the inverter-side inductors and filter capacitors are kept the same, as shown in Fig. 18. In spite of adverse distorted unbalanced grid voltages and grid frequency variation, as shown in Fig. 18(a), as well as the model uncertainty in the *LCL* filter, the steady-state grid-injected currents at 60 Hz are perfectly stable and satisfactory, as depicted in Fig. 19(a). These results are consistent with the experimental results for the *LCL*

TABLE II
EXECUTION TIME OF THE PROPOSED SENSORLESS CONTROL SCHEME

Full algorithm	88 μs
Space vector modulation + data acquisition + etc.	43 μs
Resonant extended observer (RESO)	18 μs
ADRC-based current controller	27 μs

filter designed in the low region in Fig. 13. Fig. 19(b) exhibits the transient response of the current controller with the grid frequency variation. Similar to the last two experiments, the transient response is desirably fast and injected current quality is high, which proves the effectiveness and reliability of the proposed control strategy for an *LCL*-filtered inverter system even in the presence of extremely severe operating conditions. Moreover, Fig. 19(c) shows the α-axis grid current and the estimated grid frequency $\hat{f}$, which converges well to the actual value f within a short transient period of 40 ms. This figure also displays that the estimated phase angle $\hat{\theta}$ almost overlaps with the phase angle θ obtained from the SRF-PLL.

The execution time to implement the proposed grid voltage sensorless current controller in DSP is represented for individual routines in Table II. The total execution time of the proposed control scheme takes 88% of the sampling period, which is acceptable and easily implemented with the commercial DSP.

C. Comparison

To demonstrate the improvement of the proposed optimized ADRC with the RESO method, a fair comparison with the conventional ADRC-based current control approach with ESO, as presented in [21], is conducted for *LCL*-filtered GCI. To evaluate the performance of the proposed and conventional ADRC-based methods in terms of disturbance rejection and robustness against parametric uncertainties, both the controllers are designed with the nominal *LCL* filter as $L_1 = 1.7$ mH, $L_2 = 1$ mH, and $C_f = 4.5$ μF. The current controller design is kept the same for two controllers. The ESO with one extended state, as represented in [21], is compared with the proposed RESO with two extended states and a sinusoidal disturbance model.

Fig. 20 shows the experimental results of grid-current responses with ADRC-based current controllers under severe *LCL* parameter variations to $L_1 = 3$ mH, $L_{2a} = 5$ mH, $L_{2b} = 3$ mH, $L_{2c} = 1$ mH, and $C_f = 3$ μF. Obviously, both ADRC-based current controllers successfully stabilize the system even under such system uncertainties. However, the current response in Fig. 20(a) shows distortion and a visible reference tracking error. On the other hand, the current response of the proposed grid voltage sensorless controller with RESO in Fig. 20(b) demonstrates superior performance with zero tracking error even without the grid voltage sensing devices.

The results, as shown in the above simulations and experiments, illustrate that the proposed optimized ADRC approach offers an effective and reliable operation in all test conditions no matter the elimination of the grid voltage sensors. The high performance is successfully achieved by inheriting the merits of the traditional ADRC, RESO, and resonant compensators to deal with adverse internal and external disturbances.

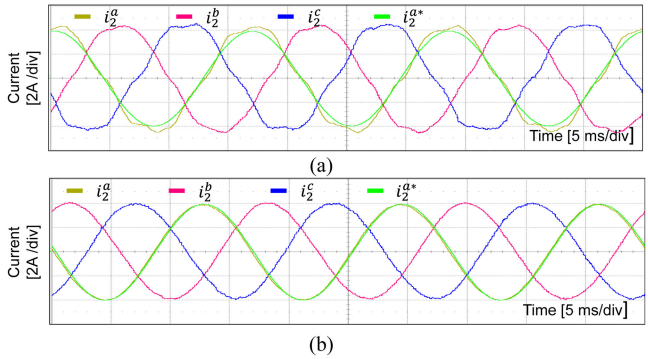

Fig. 20. Experimental results of grid-current responses with ADRC-based current controllers under the *LCL* parameter variations to $L_1 = 3$ mH, $L_{2a} = 5$ mH, $L_{2b} = 3$ mH, $L_{2c} = 1$ mH, and $C_f = 3$ μF. (a) ADRC-current controller with ESO [21]. (b) ADRC-current controller with proposed RESO.

VI. CONCLUSION

This article has presented an optimized ADRC with RESO for a grid voltage sensorless *LCL*-filtered inverter, which is subject to various sources of disturbance, including the model uncertainties, the *LCL* inherent resonance phenomenon, and external disturbances from the grid environment. To overcome the challenges induced by the digital implementation delay and disturbance in sinusoidal form, the discrete current-type RESO has been proposed to provide the estimates for both the states and lumped disturbance. By means of the generalized predictive controller and the incorporation of the harmonic compensator together with the direct disturbance rejection, an optimized tracking controller is realized. The robustness and stability of the proposed scheme have been demonstrated under internal uncertainties by the discrete-time frequency analysis and pole-zero map approaches. Moreover, through the least-mean-square-based synchronization technique, the grid information is instantly extracted from the disturbance estimation instead of the measured grid voltages. As a result, the proposed method successfully fulfills the desired control objectives by utilizing only the sensor measurements from the dc-link voltage and grid-side currents. The comprehensive simulation and experimental tests have been carried out to verify the effectiveness and feasibility of the proposed optimized ADRC with RESO for a grid voltage sensorless *LCL*-filtered inverter in several severe operation conditions.

REFERENCES

[1] R. N. Beres, X. Wang, F. Blaabjerg, M. Liserre, and C. L. Bak, "Optimal design of high-order passive-damped filters for grid-connected applications," *IEEE Trans. Power Electron.*, vol. 31, no. 3, pp. 2083–2098, Mar. 2016.

[2] C. Xie, K. Li, J. Zou, D. Liu, and J. M. Guerrero, "Passivity-based design of grid-side current-controlled LCL-type grid-connected inverters," *IEEE Trans. Power Electron.*, vol. 35, no. 9, pp. 9813–9823, Sep. 2020.

[3] B. Abdeldjabar, X. Dianguo, X. Wang, and F. Blaabjerg, "Robust active damping control of LCL filtered grid connected converter based active disturbance rejection control," in *Proc. IEEE 8th Int. Power Electron. Motion Control Conf.*, Hefei, China, 2016, pp. 2661–2666.

[4] J. Kukkola and M. Hinkkanen, "State observer for grid-voltage sensorless control of a converter under unbalanced conditions," *IEEE Trans. Ind. Appl.*, vol. 54, no. 1, pp. 286–297, Jan./Feb. 2018.
[5] E. Rodriguez-Diaz, F. D. Freijedo, J. C. Vasquez, and J. M. Guerrero, "Analysis and comparison of notch filter and capacitor voltage feedforward active damping techniques for LCL grid-connected converters," *IEEE Trans. Power Electron.*, vol. 34, no. 4, pp. 3958–3972, Apr. 2019.
[6] J. M. Gonzalez, C. A. Busada, and J. A. Solsona, "A robust controller for a grid-tied inverter connected through an LCL filter," *IEEE J. Emerg. Sel. Topics Ind. Electron.*, vol. 2, no. 1, pp. 82–89, Jan. 2021.
[7] Y. Xiong, Y. Ye, Y. Cao, and Y. Wu, "Separate-structure UDE-based current resonant control strategy on LCL-type grid-tied inverters with weighted average current method for improved injected current quality and robustness," *IEEE Trans. Power Electron.*, vol. 35, no. 12, pp. 13641–13651, Dec. 2020.
[8] W. Binbing, T. Yizhi, C. Yuxi, X. Abuduwayiti, and L. Xiong, "Virtual frequency construction-based vector current control for grid-tied inverter under imbalanced voltage," *IEEE Access*, vol. 8, pp. 199654–199663, 2020.
[9] R. Errouissi and A. Al-Durra, "Disturbance-observer-based control for dual-stage grid-tied photovoltaic system under unbalanced grid voltages," *IEEE Trans. Ind. Electron.*, vol. 66, no. 11, pp. 8925–8936, Nov. 2019.
[10] Y. Wu, Y. Ye, Q. Zhao, Y. Cao, and Y. Xiong, "Discrete-time modified UDE-based current control for LCL-type grid-tied inverters," *IEEE Trans. Ind. Electron.*, vol. 67, no. 3, pp. 2143–2154, Mar. 2020.
[11] C. R. D. Osório, G. G. Koch, H. Pinheiro, R. C. L. F. Oliveira, and V. F. Montagner, "Robust current control of grid-tied inverters affected by LCL filter soft-saturation," *IEEE Trans. Ind. Electron.*, vol. 67, no. 8, pp. 6550–6561, Aug. 2020.
[12] I. Sefa, S. Ozdemir, H. Komurcugil, and N. Altin, "An enhanced Lyapunov-function based control scheme for three-phase grid-tied VSI with LCL filter," *IEEE Trans. Sustain. Energy*, vol. 10, no. 2, pp. 504–513, Apr. 2019.
[13] N. Altin, S. Ozdemir, H. Komurcugil, and I. Sefa, "Sliding-mode control in natural frame with reduced number of sensors for three-phase grid-tied LCL-interfaced inverters," *IEEE Trans. Ind. Electron.*, vol. 66, no. 4, pp. 2903–2913, Apr. 2019.
[14] M. Su *et al.*, "Single-sensor control of LCL-filtered grid-connected inverters," *IEEE Access*, vol. 7, pp. 38481–38494, 2019.
[15] T. V. Tran and K.-H. Kim, "Frequency adaptive grid voltage sensorless control of LCL-filtered inverter based on extended model observer," *IEEE Trans. Ind. Electron.*, vol. 67, no. 9, pp. 7560–7573, Sep. 2020.
[16] V. R. Chowdhury and J. Kimball, "Robust control scheme for a three phase grid-tied inverter with LCL filter during sensor failures," *IEEE Trans. Ind. Electron.*, 2020, early access, doi: 10.1109/TIE.2020.3013515.
[17] R. Guzman, L. G. de Vicuña, M. Castilla, J. Miret, and J. de la Hoz, "Variable structure control for three-phase LCL-filtered inverters using a reduced converter model," *IEEE Trans. Ind. Electron.*, vol. 65, no. 1, pp. 5–15, Jan. 2018.
[18] X. Chen, W. Wu, N. Gao, H. S.-H. Chung, M. Liserre, and F. Blaabjerg, "Finite control set model predictive control for LCL-filtered grid-tied inverter with minimum sensors," *IEEE Trans. Ind. Electron.*, vol. 67, no. 12, pp. 9980–9990, Dec. 2020.
[19] R. Guzman, L. G. de Vicuña, M. Castilla, J. Miret, and H. Martín, "Variable structure control in natural frame for three-phase grid-connected inverters with LCL filter," *IEEE Trans. Power Electron.*, vol. 33, no. 5, pp. 4512–4522, May 2018.
[20] J. Liu, W. Wu, H. S.-H. Chung, and F. Blaabjerg, "Disturbance observer-based adaptive current control with self-learning ability to improve the grid-injected current for LCL-filtered grid-connected inverter," *IEEE Access*, vol. 7, pp. 105376–105390, 2019.
[21] B. Wang, Z. Shen, H. Liu, and J. Hu, "Linear ADRC direct current control of grid-connected inverter with LCL filter for both active damping and grid voltage induced current distortion suppression," *IET Power Electron.,* vol. 11, no. 11, pp. 1748–1755, Sep. 2018.
[22] A. Benrabah, D. Xu, and Z. Gao, "Active disturbance rejection control of LCL-filtered grid-connected inverter using Padé approximation," *IEEE Trans. Ind. Appl.*, vol. 54, no. 6, pp. 6179–6189, Nov./Dec. 2018.
[23] J. Han, "From PID to active disturbance rejection control," *IEEE Trans. Ind. Electron.*, vol. 56, no. 3, pp. 900–906, Mar. 2009.
[24] Z. Gao, "Scaling and bandwidth-parameterization based controller tuning," in *Proc. Amer. Control Conf.*, Denver, CO, USA, 2003, pp. 4989–4996.
[25] W. Ma, Y. Guan, B. Zhang, and L. Wu, "Active disturbance rejection control based single current feedback resonance damping strategy for LCL-type grid-connected inverter," *IEEE Trans. Energy Convers.*, vol. 36, no. 1, pp. 48–62, Mar. 2021.
[26] J. Lu, M. Savaghebi, J. M. Guerrero, J. C. Vasquez, and C. Xie, "Linear active disturbance rejection control for LCL type grid-connected converter," in *Proc. 42th Annu. Conf. IEEE Ind. Electron. Soc.*, Florence, Italy, 2016, pp. 3458–3463.
[27] T. Minghe, W. Bo, Y. Yong, M. Xing, D. Qinghua, and X. Dianguo, "Proportional resonant-based active disturbance rejection control for speed fluctuation suppression of PMSM drives," in *Proc. 22nd Int. Conf. Elect. Mach. Syst.*, Harbin, China, 2019, pp. 1–6.
[28] R. Miklosovic, A. Radke, and Z. Gao, "Discrete implementation and generalization of the extended state observer," in *Proc. Amer. Control Conf.*, Minneapolis, MN, USA, 2006, pp. 2209–2214.
[29] R. Madonski and P. Herman, "Survey on methods of increasing the efficiency of extended state disturbance observers," *ISA Trans.,* vol. 56, pp. 18–27, 2015.
[30] M. R. Stankovic, M. R. Rapaic, S. M. Manojlovic, S. T. Mitrovic, S. M. Simic, and M. B. Naumovic, "Optimised active disturbance rejection motion control with resonant extended state observer," *Int. J. Control*, vol. 92, no. 8, pp. 1815–1826, 2019.
[31] W.-H. Chen, D. J. Ballance, and P. J. Gawthrop, "Optimal control of nonlinear systems: A predictive control approach," *Automatica*, vol. 39, no. 4, pp. 633–641, Apr. 2003.
[32] J. Yang, H. Cui, S. Li, and A. Zolotas, "Optimized active disturbance rejection control for DC-DC buck converters with uncertainties using a reduced-order GPI observer," *IEEE Trans. Circuits Syst. I, Reg. Papers*, vol. 65, no. 2, pp. 832–841, Feb. 2018.
[33] Y. Yan, J. Yang, C. Liu, M. Coombes, S. Li, and W.-H. Chen, "On the actuator dynamics of dynamic control allocation for a small fixed-wing UAV with direct lift control," *IEEE Trans. Control Syst. Technol.*, vol. 28, no. 3, pp. 984–991, May 2020.
[34] R. Teodorescu, M. Liserre, and P. Rodriguez, *Grid Converters for Photovoltaic and Wind Power Systems*. Chichester, U.K.: Wiley, 2010.
[35] T. V. Tran, M. Kim, and K.-H. Kim, "Frequency adaptive current control scheme for grid-connected inverter without grid voltage sensors based on gradient steepest descent method," *Energies*, vol. 12, no. 22, Nov. 2019, Art. no. 4266.
[36] D. P. Bertsekas, *Nonlinear Programming*, 2nd ed. Athena Sci.: Belmont, MA, USA, 1999.
[37] W. Tan and C. Fu, "Linear active disturbance-rejection control: Analysis and tuning via IMC," *IEEE Trans. Ind. Electron.*, vol. 63, no. 4, pp. 2350–2359, Apr. 2016.
[38] Y. Cao, Q. Zhao, Y. Ye, and Y. Xiong, "ADRC-based current control for grid-tied inverters: Design, analysis, and verification," *IEEE Trans. Ind. Electron.*, vol. 67, no. 10, pp. 8428–8437, Oct. 2020.

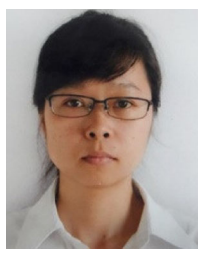

Thuy Vi Tran was born in Ba Ria Vung Tau, Vietnam, in 1991. She received the B.S. degree in electrical engineering from Portland State University, Portland, OR, USA, in 2014, and the M.S. degree in electrical and information engineering in 2020 from the Seoul National University of Science and Technology, Seoul, South Korea, where she is currently working toward the Ph.D. degree with the Department of Electrical and Information Engineering.

Her research interests include robust control, renewable energy, and power electronics.

Kyeong-Hwa Kim (Senior Member, IEEE) was born in Seoul, South Korea, in 1969. He received the B.S. degree from Hanyang University, Seoul, South Korea, in 1991, and the M.S. and Ph.D. degrees from the Korea Advanced Institute of Science and Technology (KAIST), Daejeon, South Korea, in 1993 and 1998, respectively, all in electrical engineering.

From 1998 to 2000, he was a Research Engineer with Samsung Electronics Company, South Korea, where he was engaged in the research and development of ac machine drive systems. From 2000 to 2002, he was a Research Professor with KAIST, and from August 2010 to August 2011, a Visiting Scholar with the Virginia Polytechnic Institute and State University (Virginia Tech), Blacksburg, VA, USA. Since August 2002, he has been with the Seoul National University of Science and Technology, Seoul, South Korea, where he is currently a Professor. His current research interests include ac machine drives, the control and diagnosis of power systems, power electronics, renewable energy, and digital signal processing based control applications.

Dr. Kim is a member of the Korean Institute of Power Electronics.

Jih-Sheng (Jason) Lai (Life Fellow, IEEE) received the M.S. and Ph.D. degrees in electrical engineering from the University of Tennessee, Knoxville, TN, USA, in 1985 and 1989, respectively.

In 1989, he joined Electric Power Research Institute (EPRI) Power Electronics' Applications Center (PEAC), where he managed EPRI-sponsored power electronics research projects; in 1993, Oak Ridge National Laboratory as a Power Electronics Lead Scientist, where he initiated a high-power electronics program and developed several novel high power converters, including multilevel converters and soft-switching inverters; and in 1996, Virginia Polytechnic Institute and State University. He is currently the James S. Tucker Professor with the Department of Electrical and Computer Engineering and the Director of Future Energy Electronics Center. He also holds Visiting Mount-Jade Chair Professorship with National Yang Ming Chiao Tong University, Taiwan, and serves as a Visiting Professor with Nanyang Technological University, Singapore. His main research areas focus on high-efficiency power electronics' conversions for high power and energy applications. He has authored or coauthored more than 490 refereed technical papers, one book chapter, two books, and 30 patents.

Dr. Lai was a recipient of the Technical Achievement Award in Lockheed Martin Award Night, two Journal Paper Awards, 13 Best Paper Awards from the IEEE-sponsored conferences, and the 2016 IEEE IAS Gerald Kliman Innovator Award. He led the student teams to win the Top Three Finalist in Google Little Box Challenge in 2016, Grand Prize Award from International Future Energy Challenge (IFEC) in 2011, and Grand Prize Award from Texas Instruments Engibous Analog Design Competition in 2009. He is the Founding Chair of 2001 IEEE IFEC and 2016 IEEE ACEPT, and General Chair of IEEE COMPEL-2000, IEEE APEC 2005, IEEE SPEC-2018, IEEE IFEEC-2019, and IEEE STPEC-2020 conferences.